

Stabilizing Transient Disturbances With Utility-Scale Inverter-Based Resources

Ryan T. Elliott
ryanelliott@ieee.org

Payman Arabshahi
paymana@uw.edu

Daniel S. Kirschen
kirschen@uw.edu

Department of Electrical and Computer Engineering
University of Washington

November 30th 2020

Abstract

This paper presents a trajectory tracking control strategy that modulates the active power injected by geographically distributed inverter-based resources to support transient stability. Each resource is independently controlled, and its response drives the local bus voltage angle toward a trajectory that tracks the angle of the center of inertia. The center-of-inertia angle is estimated in real time from wide-area measurements. The main objectives are to stabilize transient disturbances and increase the amount of power that can be safely transferred over key transmission paths without loss of synchronism. Here we envision the actuators as utility-scale energy storage systems; however, equivalent examples could be developed for partially-curtailed photovoltaic generation and/or Type 4 wind turbine generators. The strategy stems from a time-varying linearization of the equations of motion for a synchronous machine. The control action produces synchronizing torque in a special reference frame that accounts for the motion of the center of inertia. This drives the system states toward the desired trajectory and promotes rotor angle stability. For testing we employ a reduced-order dynamic model of the North American Western Interconnection. The results show that this approach improves system reliability and can increase capacity utilization on stability-limited transmission corridors.

1 Introduction

When power systems that lack sufficient synchronizing torque are subjected to a severe disturbance they may fail to maintain rotor angle stability. To mitigate this risk, stability limits are imposed on certain transmission corridors that inhibit the full utilization of existing thermal capacity. In turn, this increases the investment and operation costs of the transmission system. While power system stabilizers and turbine governors do respond to large disturbances, their chief objective

*This is a preprint of a paper accepted by IET Generation, Transmission, & Distribution and is subject to Institution of Engineering and Technology Copyright. When the final version is published, the copy of record will be available at the IET Digital Library.

is not to maintain first swing transient stability. With the exception of voltage regulation, engineers have generally turned to protection and remedial action schemes to maintain transient stability rather than feedback control systems [1]. The challenges of implementing the latter are twofold. First, stabilizing transient disturbances requires actuators that can rapidly respond to events such as faults, line outages, and generator trips. Second, as the system is pushed further away from its original stable equilibrium, constructing a suitable feedback signal solely from local information becomes increasingly difficult [2]. The combination of wide-area measurement systems (WAMS) and fast-acting inverter-based resources (IBRs) enables new approaches to address these problems.

In this paper, we develop and demonstrate a trajectory tracking control strategy for stabilizing transient disturbances. It modulates the active power injected by independently controlled, geographically distributed IBRs. The controllers are independent in the sense that they each synthesize their own wide-area reference and calculate their own control error and corresponding injection. Here we envision the actuators as utility-scale energy storage systems (ESS). The response of each actuator drives its local bus voltage angle toward a trajectory that tracks an estimate of the angle of the center of inertia synthesized from WAMS data. The overall strategy arises from a time-varying linearization of the equations of motion for a synchronous machine. The control response produces synchronizing torque in a special reference frame that accounts for the motion of the center of inertia. This drives the system states toward the desired nonequilibrium trajectory and promotes rotor angle stability. For testing, we employ a reduced-order dynamic model of the North American Western Interconnection called the *miniWECC* [3]. The results show that this control strategy improves system reliability and can increase capacity utilization on stability-limited transmission corridors.

1.1 Literature Review

From a systems theory perspective, transient stability pertains to stability in the sense of Lyapunov. Hence, it cannot be completely determined using linear analysis. One of the oldest and most important techniques for assessing transient stability is the *equal area criterion*. This graphical method provides valuable intuition about transient disturbances; however, its scope is limited to two-machine systems and the classical single-machine infinite bus framework. To address these limitations, alternative methods were sought that could be applied to more complex networks of synchronous machines. In [4], Xue et al. developed what they called the *extended equal area criterion*, which was based upon a two-machine equivalent model of the system. In parallel, there was a movement toward *direct methods* of determining transient stability, which do not require the solution of the differential equations, i.e., simulated trajectories [5, 6]. Inspired by the efforts of Magnusson in [7], energy-based methods for stability analysis were developed and refined in [8–12].

Athay et al. put forth a seminal application of energy function analysis in [8]. They developed a system-wide energy function that accounted for the total change in rotor kinetic energy and potential energy. While useful, system-wide energy functions did not always provide insight into the mechanism of instability, or which critical machines, if any, were susceptible to loss of synchronism. Motivated by these factors, Vittal developed energy functions for individual machines using the concept of partial stability in [10]. The theory of partial energy functions was further extended in [13]. As described in Section 13.7 of [14], limitations related to model accuracy and computational reliability impeded the adoption of direct methods in practice, but many core ideas were revisited in the context of *hybrid methods*. The defining characteristic

of hybrid methods is that they combine energy function analysis with traditional time-domain simulation [15–17]. This approach sidesteps some of the challenges associated with direct methods while streamlining the process of determining stability margins. In Section 4, we use a hybrid approach inspired by [17] to study the impact of the proposed control strategy on system faults. Work continues on the subject of direct methods, with recent examples including [18, 19]. For further recent developments in transient stability assessment, see [20–22].

Numerous protection and remedial action schemes (RAS) have been developed to bolster transient stability [23–26]. Also called *system protection schemes*, RAS initiate a predetermined action, or sequence thereof, in response to a particular condition or event [1]. In contrast, feedback control systems modulate the output of one or more actuators in response to an error signal. A majority of the control systems developed for transient stability regulate bus voltages using synchronous machine excitation systems and/or FACTS devices [27, 28]. Related applications for series devices have also been explored [29, 30]. Driven by economic and environmental factors, many contemporary large-scale power systems are experiencing rapid growth in the number of inverter-based resources. As the penetration of IBRs has grown, so too has interest in their potential to support transient stability [31, 32]. In this work, we present a control strategy designed to stabilize transient disturbances by modulating the active power injected by IBRs. Examples of suitable actuators include energy storage systems and partially-curtailed photovoltaic generation.

1.2 Paper Organization

The remainder of this paper is organized as follows. Section 2 presents a time-varying linearization of the equations of motion for a synchronous machine. We then derive a trajectory tracking control strategy that emerges from this framework. In Section 3, we examine a set of large-scale sensitivity studies based on a reduced-order dynamic model of the Western Interconnection. Section 4 outlines the lessons learned from N-1 contingency analysis. In Section 5, we discuss a simplified path rating study for the California-Oregon Intertie. Section 6 summarizes and concludes.

2 Proposed Method

We base the wide-area control strategy on a time-varying linearization of the equations of motion for a synchronous machine. The accuracy of classical linear time-invariant (LTI) models tends to decrease when the system operating point is driven away from the initial equilibrium. Linearizing the system dynamics around an appropriately selected trajectory can improve model accuracy under transient disturbances [33,34]. This section provides a primer on the definitions and theory of continuous-time linear time-varying (LTV) systems. It then presents a derivation showing how the control strategy arises from these conceptual foundations.

2.1 Mathematical Preliminaries

Let $f : \mathbb{R}^n \times \mathbb{R}^m \rightarrow \mathbb{R}^n$ denote a nonlinear vector field

$$\dot{x}(t) = f(x(t), u(t)), \quad (1)$$

where $x(t) \in \mathbb{R}^n$ is the system state at time t and $u(t) \in \mathbb{R}^m$ the input. Linearizing f about a static equilibrium $\{x_0, u_0\}$ produces a linear time-invariant system representation. Alternatively, linearizing about a nonequilibrium trajectory $\{\bar{x}(t), \bar{u}(t)\}$ produces a linear time-varying representation

$$\Delta\dot{x}(t) = A(t)\Delta x(t) + B(t)\Delta u(t), \quad (2)$$

where $\Delta x(t) = x(t) - \bar{x}(t)$ and $\Delta u(t) = u(t) - \bar{u}(t)$. As explained in [35], the state-space matrices in (2) are functions of time

$$A(t) = D_x f(\bar{x}(t), \bar{u}(t)) \quad (3)$$

$$B(t) = D_u f(\bar{x}(t), \bar{u}(t)), \quad (4)$$

where the operator D_x returns the Jacobian matrix of partial derivatives with respect to x evaluated at time t , and D_u returns the analogous matrix of partials with respect to u .

2.2 Control Strategy Derivation

In this section, we derive a trajectory tracking control strategy by applying the concepts introduced in Section 2.1. Table 1 provides an overview of the mathematical notation used throughout the derivation. Consider a synchronous machine connected to a large power system. In terms of per-unit accelerating power, the nonlinear equations of motion may be expressed as

$$\dot{\delta}(t) = \omega_b[\omega(t) - \omega_0] \quad (5)$$

$$\dot{\omega}(t) = -\frac{D}{2H}[\omega(t) - \omega_0] + \frac{1}{2H\omega(t)}[P_m(t) - P_e(t)], \quad (6)$$

where ω_0 is the per-unit synchronous speed, and $\omega_b = 2\pi f_0$ is the per-unit electrical speed base, where f_0 is the nominal system frequency. The machine damping coefficient is denoted by D , and the inertia constant by H . Recall that (5) describes the angular velocity of the rotor and (6) the acceleration. Now let $\mathfrak{D}(t)$ and $\mathfrak{T}(t)$ be time-varying coefficients defined as

$$\begin{bmatrix} \mathfrak{D}(t) \\ \mathfrak{T}(t) \end{bmatrix} \triangleq -2H \begin{bmatrix} \frac{\partial \dot{\omega}}{\partial \omega} \\ \frac{\partial \dot{\omega}}{\partial \delta} \end{bmatrix} \bigg|_{\bar{x}(t), \bar{u}(t)}, \quad (7)$$

Table 1: Mathematical Notation

Symbol	Meaning	Units
$\delta(t)$	rotor angle	elect. rad
$\tilde{\delta}(t)$	center-of-inertia angle	elect. rad
$\bar{\delta}_i(t)$	desired angle trajectory	elect. rad
$\omega(t)$	rotor speed	pu
$\tilde{\omega}(t)$	center-of-inertia speed	pu
$\bar{\omega}_i(t)$	desired speed trajectory	pu
ω_b	speed base	rad s ⁻¹
ω_0	synchronous speed	pu
$\theta(t)$	bus voltage angle	rad
$\tilde{\theta}(t)$	wide-area angle reference	rad
$\bar{\theta}_j(t)$	desired bus voltage angle trajectory	rad
$f(t)$	bus frequency	Hz
$\tilde{f}(t)$	center-of-inertia frequency	Hz
$\bar{f}_j(t)$	desired bus frequency trajectory	Hz
$P_m(t)$	mechanical power	pu
$P_e(t)$	electrical power	pu
H	inertia constant	s
D	LTI damping coefficient	pu
\mathfrak{D}	LTV damping coefficient	pu
\mathfrak{T}	LTV synchronizing coefficient	pu
γ_k	sensor weights	–
α_1, α_2	tuning parameters	–
$\Delta\xi(t)$	control error	–
i	synchronous machine index	–
j	actuator index	–
k	sensor index	–

where the right-hand side represents the scaled partial derivatives of (6) taken with respect to the state variables ω and δ . These derivatives are evaluated about a state trajectory $\bar{x}(t)$ and input $\bar{u}(t)$. We show that when $\bar{x}(t)$ is selected appropriately, $\mathfrak{D}(t)$ is the damping coefficient in the center-of-inertia reference frame and $\mathfrak{T}(t)$ the synchronizing torque coefficient. For analysis of the LTV damping coefficient $\mathfrak{D}(t)$, see [33].

The appropriate analytical form of $\mathfrak{T}(t)$ depends on the model being used to describe transmission network. In the special case of a single-machine infinite bus system, the electrical power output of the machine is given by

$$P_e(t) = \frac{EV}{X} \sin \delta(t), \quad (8)$$

where X is the sum of the synchronous reactance and the line reactance between the terminals of the machine and the infinite bus. The internal stator voltage magnitude is denoted by E and

the voltage magnitude at the infinite bus by V . Per convention, the infinite bus has a voltage angle of zero. Evaluating (7), the LTV synchronizing torque coefficient is

$$\mathfrak{T}(t) = \frac{EV \cos \bar{\delta}(t)}{X \bar{\omega}(t)}, \quad (9)$$

where $\bar{\omega}(t)$ and $\bar{\delta}(t)$ specify the nonequilibrium state trajectory generically represented as $\bar{x}(t)$. The expression in (9) could be readily modified to accommodate a third-order Heffron-Phillips model by allowing the internal stator voltage to vary with time. In the context of multi-machine models such as those described in [5], $\mathfrak{T}(t)$ follows from (7).

Linearizing (5) and (6) about a trajectory and expressing the result in terms of $\mathfrak{D}(t)$ and $\mathfrak{T}(t)$ yields

$$\Delta \dot{\delta}(t) = \omega_b \Delta \omega(t) \quad (10)$$

$$\Delta \dot{\omega}(t) = -\frac{\mathfrak{D}(t)}{2H} \Delta \omega(t) - \frac{\mathfrak{T}(t)}{2H} \Delta \delta(t) + \frac{1}{2H \bar{\omega}(t)} \Delta P_m(t), \quad (11)$$

where the state deviations are given by $\Delta \delta(t) = \delta(t) - \bar{\delta}(t)$ and $\Delta \omega(t) = \omega(t) - \bar{\omega}(t)$. Recall that $\bar{\delta}(t)$ denotes the nonequilibrium angle trajectory, and $\bar{\omega}(t)$ the speed trajectory. Furthermore, $\Delta P_m(t) = P_m(t) - \bar{P}_m(t)$, where $\bar{P}_m(t)$ is the mechanical power input trajectory. As shown in [33, 34], it is possible to increase damping and support small-signal stability by producing electrical torque that is in phase with the speed deviation between the rotor and the center of inertia. Here we develop a strategy for stabilizing transient disturbances that produces an electrical power injection that is in phase with $\Delta \delta(t)$.

2.3 Nonequilibrium Trajectory

The nonequilibrium trajectory about which the equations of motion are linearized is based on a real-time estimate of the angle of the center of inertia. The concept of the center of inertia was introduced in [36] to facilitate a decomposition of the system dynamics. This decomposition allowed for precise characterization of the system frequency and synchronous equilibria. Let h_i be the normalized inertia constant for the i th machine

$$h_i = \frac{H_i}{H_T} \quad H_T = \sum_{i \in \mathcal{I}} H_i, \quad (12)$$

where \mathcal{I} is the set of all online synchronous machines. The center-of-inertia speed and angle are then defined such that

$$\tilde{\omega}(t) = \sum_{i \in \mathcal{I}} h_i \omega_i(t) \quad (13)$$

$$\tilde{\delta}(t) = \sum_{i \in \mathcal{I}} h_i \delta_i(t). \quad (14)$$

Let $\{\bar{\delta}_i(t), \bar{\omega}_i(t)\}$ be the nonequilibrium state trajectory. In the control strategy, $\bar{\delta}_i(t)$ represents the desired angle trajectory toward which unit i is driven.

As explained in [10], the transient kinetic energy responsible for the separation of one or more generators from the rest of the system originates from the motion of the critical group of machines away from the center of inertia. Hence, following a disturbance, driving the speed

of each generator back toward the speed of the center of inertia serves to reduce this transient kinetic energy and mitigate the risk of separation (see Section 4). The nonequilibrium speed trajectory corresponding to this strategy is

$$\bar{\omega}_i(t) = \tilde{\omega}(t), \quad (15)$$

for all i in \mathcal{I} . Because the rotor speed and angle are dynamically linked, (15) has implications for the angle trajectory $\bar{\delta}_i(t)$. From (5), the center-of-inertia angle $\tilde{\delta}(t)$ and the desired angle trajectory $\bar{\delta}_i(t)$ may be stated as

$$\tilde{\delta}(t) = \tilde{\delta}(t_0) + \omega_b \int_{t_0}^t \tilde{\omega}(\tau) - \omega_0 d\tau \quad (16)$$

$$\bar{\delta}_i(t) = \bar{\delta}_i(t_0) + \omega_b \int_{t_0}^t \bar{\omega}_i(\tau) - \omega_0 d\tau. \quad (17)$$

As a result of (15), we may restate (17) in terms of $\tilde{\omega}(t)$

$$\bar{\delta}_i(t) = \bar{\delta}_i(t_0) + \omega_b \int_{t_0}^t \tilde{\omega}(\tau) - \omega_0 d\tau. \quad (18)$$

The center-of-inertia speed appears in the integrand of both (16) and (18) because $\bar{\omega}_i(t) = \tilde{\omega}(t)$ for all $i \in \mathcal{I}$.

Recall that the LTV angle deviation of the i th machine is defined as $\Delta\delta_i(t) = \delta_i(t) - \bar{\delta}_i(t)$. In order for the angle deviation to be zero in steady state, it must hold that

$$\bar{\delta}_i(t_0) = \delta_i(t_0), \quad (19)$$

where t_0 indicates a point in time where the system resides at a stable equilibrium. As a consequence of (19), $\bar{\delta}_i(t)$ is, in general, different for each unit. Combining (16), (18), and (19) to solve for the nonequilibrium angle trajectory yields

$$\bar{\delta}_i(t) = \tilde{\delta}(t) - \tilde{\delta}(t_0) + \delta_i(t_0). \quad (20)$$

Hence, $\bar{\delta}_i(t)$ is equal to the angle of the center of inertia plus a fixed offset $\delta_i(t_0) - \tilde{\delta}(t_0)$. This offset represents the difference between the rotor angle of the i th unit and the angle of the center of inertia at the stable equilibrium observed at t_0 . Thus, the nonequilibrium state trajectory $\{\bar{\delta}_i(t), \bar{\omega}_i(t)\}$ is fully described by (15) and (20).

2.4 Real-Time Trajectory Estimation

In a real-time control application, the center-of-inertia angle $\tilde{\delta}(t)$ would need to be estimated using available measurements. The challenges posed by this problem fall mostly outside the scope of this paper; however, we will discuss some core concepts here. At the time of this writing, rotor angle measurements are not generally available through wide-area measurement systems. Thus, it is not possible to directly calculate (14) onboard the controller. If a suitable estimate of the center-of-inertia speed is available, $\tilde{\delta}(t)$ may be approximated as

$$\tilde{\delta}(t) \approx c + \omega_b \int_{t_0}^t \tilde{\omega}(\tau) - \omega_0 d\tau, \quad (21)$$

where c is a constant. In practice, (21) would be computed using numerical integration. In this paper, we synthesize the center-of-inertia angle estimates by approximating (14) with a weighted average of bus voltage angle measurements

$$\tilde{\delta}(t) \approx c + \sum_{k \in \mathcal{K}} \gamma_k \theta_k(t). \quad (22)$$

In (22), $\theta_k(t)$ is the angle measurement signal reported by the k th sensor, γ_k the associated weight, and \mathcal{K} the set of available sensors. The weights γ_k are nonnegative and sum to one, i.e., $\mathbf{1}^T \boldsymbol{\gamma} = 1$. These weights do not necessarily correspond to physical quantities. They may be thought of as optimization variables in a problem where the objective is to minimize the norm of the difference between the estimated and actual center-of-inertia angle signals. For simplicity, we consider the arithmetic mean $\gamma_k = 1/|\mathcal{K}|$ for all k , where $|\mathcal{K}|$ is the number of available sensors. The key outcomes of this paper do not depend strongly on this choice.

In the controller, the value of c in (22) is of little importance because the offset in (20) ensures that $\Delta\delta_i(t_0) = 0$. Thus, we may henceforth regard c as a free parameter or set it to zero. Given nonideal sensors, the approach in (22) may be slightly more susceptible to measurement bias than (21); however, the dc offset of the reference signal is not critical in this application, as noted above. No generator measurements or data are required to implement the control strategy. All of the required measurements could be made by commercially available phasor measurement units (PMUs) as described in [37]. In practice, radian phase angle measurements are typically mapped onto the interval $(-\pi, \pi]$. Using this system, small physical changes may manifest themselves as large numerical changes when an angle wraps around the discontinuity at $-\pi$. Thus, all phase angle measurements must be properly unwrapped when estimating $\tilde{\delta}(t)$ using (22). Failure to do so could propagate discontinuities associated with angle wrapping into the control error itself. For more information on wide-area phase angle calculations, see [38].

2.5 Control Structure Refinement

Many synchronous machine excitation systems possess the bandwidth necessary to produce a field current modulation that is in phase with $\Delta\delta_i(t)$; however, doing so may interfere with the coordination between the automatic voltage regulator and power system stabilizer. Hence, we will explore using inverter-based resources as the control actuators. In light of this, we restrict the feedback to bus voltage angle measurements rather than rotor angles. Let $\theta_j(t)$ be the local voltage angle measured at the j th actuator at time t . The wide-area angle reference $\tilde{\theta}(t)$ is

$$\tilde{\theta}(t) = \sum_{k \in \mathcal{K}} \gamma_k \theta_k(t), \quad (23)$$

where $\gamma_k = 1/|\mathcal{K}|$, which follows from (22). We specify the desired angle trajectory for the j th actuator as

$$\bar{\theta}_j(t) = \tilde{\theta}(t) - \tilde{\theta}(t_0) + \theta_j(t_0). \quad (24)$$

This equation follows from the same reasoning as (20). The difference is that rather than beginning with the definition of a desired speed trajectory, we begin by specifying a frequency trajectory

$$\bar{f}_j(t) = \tilde{f}(t), \quad (25)$$

where $\tilde{f}(t)$ is the frequency of the center of inertia. This small modification is required because the IBRs are not necessarily co-located with synchronous machines.

In the examples given in this paper, $\tilde{\theta}(t)$ was synthesized from measurements reported by 36 simulated sensors distributed throughout the Western Interconnection. Of these, 19 were co-located with the actuators, leaving 17 additional sensors distributed throughout the system at other locations. We envision the sensors as PMUs located at high-voltage substations. Each sensor was modeled as a first-order time constant with $T = 0.02$ s. The effects of measurement noise and nonideal communication are considered in Section 4.

Given an appropriate choice of sign, (11) suggests that synchronizing torque can be produced by injecting real power that is in phase with $\Delta\theta_j(t) = \theta_j(t) - \bar{\theta}_j(t)$. By analyzing the LTI state deviations we can identify a control structure that is responsive not only to $\Delta\theta_j(t)$, but also to the movement of the center-of-inertia angle away from its predisturbance value. The LTI state deviations may be decomposed into two parts where one component captures the difference between the state and a time-varying reference, and the other the difference between the reference and its predisturbance value. The first step in this procedure is to restate the LTI control error $\theta_j(t) - \theta_j(t_0)$ in a manner that incorporates the desired angle trajectory $\bar{\theta}_j(t)$

$$\theta_j(t) - \theta_j(t_0) = \theta_j(t) - \theta_j(t_0) + \bar{\theta}_j(t) - \bar{\theta}_j(t) \quad (26)$$

$$\theta_j(t) - \theta_j(t_0) = [\theta_j(t) - \bar{\theta}_j(t)] + [\bar{\theta}_j(t) - \theta_j(t_0)]. \quad (27)$$

The first term on the right-hand side of (27) corresponds precisely to the LTV angle deviations $\Delta\theta_j(t)$, and the second makes it possible for the controller to respond to the motion of the reference trajectory away from the predisturbance equilibrium. If these two terms are weighted equally, the control error matches the LTI angle deviations; however, we may instead define the control error $\Delta\xi(t)$ as a linear combination of the two components

$$\Delta\xi(t) \triangleq \alpha_1 [\theta_j(t) - \bar{\theta}_j(t)] + \alpha_2 [\bar{\theta}_j(t) - \theta_j(t_0)], \quad (28)$$

where α_1 and α_2 are tuning parameters restricted to the unit interval. These parameters provide the ability to tune the magnitude of the open-loop frequency response in two distinct frequency bands, one low and one high. We examine the relative impact of these parameters in greater detail in Section 3.

Rearranging (24), we see that

$$\bar{\theta}_j(t) - \theta_j(t_0) = \tilde{\theta}(t) - \tilde{\theta}(t_0). \quad (29)$$

By substitution, the control error $\Delta\xi(t)$ in (28) may then be restated as

$$\Delta\xi(t) = \alpha_1 [\theta_j(t) - \bar{\theta}_j(t)] + \alpha_2 [\tilde{\theta}(t) - \tilde{\theta}(t_0)]. \quad (30)$$

This form makes it clear that the second term represents the deviation between the center-of-inertia angle and its predisturbance value. As a consequence, this component of the control error is theoretically the same for all controllers. In practice, there may be small differences arising from variation in the estimates of $\tilde{\theta}(t)$.

The final structure of the wide-area synchronizing controller is shown in Fig. 1. The upper sum at the input yields the component of the control error multiplied by α_1 , and the lower sum the component multiplied by α_2 . There are two separate compensation paths, each consisting of

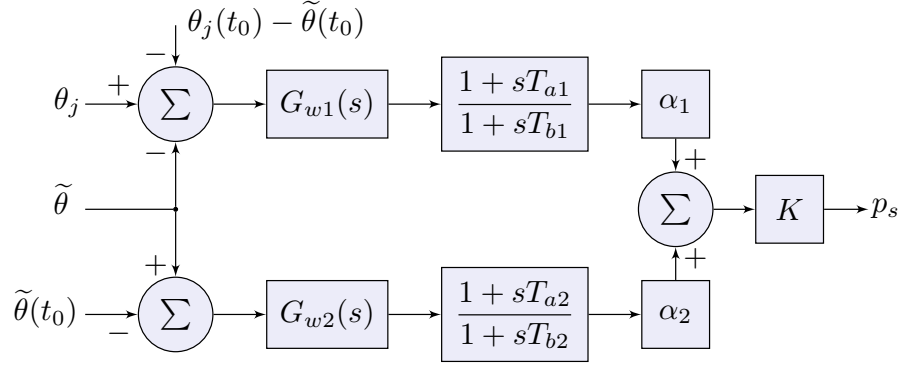


Figure 1: Block diagram of the trajectory tracking wide-area synchronizing controller. The $G_{w1}(s)$ and $G_{w2}(s)$ blocks represent washout (highpass) filters. The lead-lag compensation blocks are only used if necessary and may possess any number of stages.

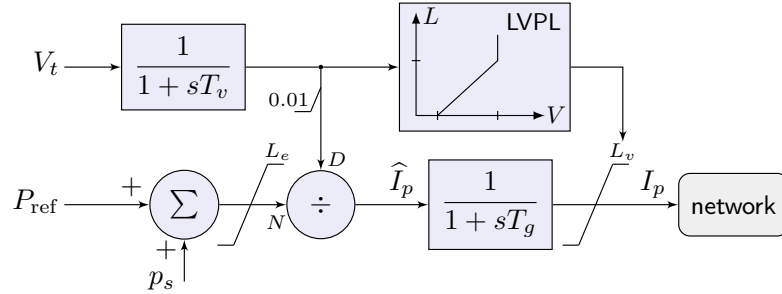


Figure 2: High-level diagram of the simplified converter interface. In the division operator N stands for numerator and D for denominator. The lower bound on the terminal voltage measurement prevents numerical errors and excessively large current commands. The *low-voltage power logic* (LVPL) block determines voltage-dependent bounds on the injected current.

a washout (highpass) filter cascaded with a lead-lag compensator. The form of the filtering and phase compensation blocks is flexible, and multiple stages may be employed if necessary. Tuning considerations are discussed in Section 3. In the case of energy storage, p_s represents a change in the charging setpoint for positive values of K .

2.6 Converter Interface Description

Fig. 2 shows a converter interface where for simplicity it is assumed that the IBR injects only active power. It is possible for the IBRs to simultaneously regulate voltage by also modulating reactive power; however, that functionality has been omitted to better illustrate the behavior of the proposed control strategy. The electrical controller shown in Fig. 1 provides an auxiliary input p_s to this interface. The structure in Fig. 2 was based on the generic dynamic models for renewable energy systems developed in the Western Electric Coordinating Council (WECC) [39].

Here P_{ref} denotes the real power setpoint of the IBR, i.e., the desired baseline injection corresponding to non-control objectives. The signal p_s represents the active power modulation command computed by the controller in Fig. 1. In the saturation stage after the initial sum, the bounds L_e on the commanded power account for device ratings and limits on the ESS state of

charge. The commanded power is then divided by the terminal voltage magnitude V_t to produce an active current command, \widehat{I}_p . In this step, a lower bound is placed on the voltage measurement to prevent numerical errors and excessively large current commands. After accounting for the interface time constant, the current command is passed through a final saturation stage where the bounds L_v are voltage dependent. This prevents the model from attempting to inject substantial active current into a faulted bus. For more information about this *low-voltage power logic* (LVPL), see [39]. In simulation, the output of the interface model specifies a boundary current injection I_p for the network equations.

2.7 Implementation Issues

The primary challenges associated with the implementing the control strategy developed here revolve around constructing a real-time estimate of the angle of the center of inertia. Contemporary PMU networks are technologically capable of enabling this estimation; however, logistical challenges remain. For instance, operating entities may be disinclined to use wide-area measurements recorded outside of their service territory for real-time control [40]. The reasons for this are mostly related to policy compliance and cybersecurity [41]. These issues are barriers to implementation for wide-area control generally and are not specific to the strategy developed in this paper. Further implementation considerations include:

- Simulation of full-scale, high-fidelity base cases to illuminate any issues potentially missed by reduced-order models;
- Analysis of issues such as multi-service provision and non-unity power factor operation of the IBRs;
- Analysis of the trade-offs associated with estimating the center-of-inertia angle locally vs. centrally, i.e., at a control center;
- Design of schemes to ensure the integrity and accuracy of the wide-area measurements, including GPS time signals;
- Design of supervisory control to ensure that the wide-area control strategy is operating as intended [42].

3 Large-Scale Sensitivity Studies

To further explore the control strategy introduced in Section 2, we present a collection of large-scale sensitivity studies. For simulation and dynamic analysis, we employ the MATLAB-based Power System Toolbox (PST) [43]. A custom dynamic model based on the diagrams shown in Figs. 1 and 2 was implemented within the PST framework. The test case is based on a reduced-order dynamic model of the Western Interconnection called the miniWECC [3]. The augmented version of the miniWECC employed here comprises 141 buses, 190 ac branches, 2 HVDC lines, and 34 synchronous generators. A total of 19 geographically distributed energy storage systems were installed in the miniWECC, one at each load center. Fig. 3 shows a map of notable locations in the system. The numbered circles indicate equivalent generators, and the colored squares indicate energy storage systems. Each generator is represented using a subtransient reactance model and a compound source rectifier exciter. Inputs to the exciter are provided by an automatic voltage regulator (AVR) and $\Delta\omega$ power system stabilizer (PSS). Turbine governors are also represented, taking into account differences between thermal and hydroelectric units. In the analysis performed here, the active component of the system load is modeled as constant current and the reactive component as constant impedance.

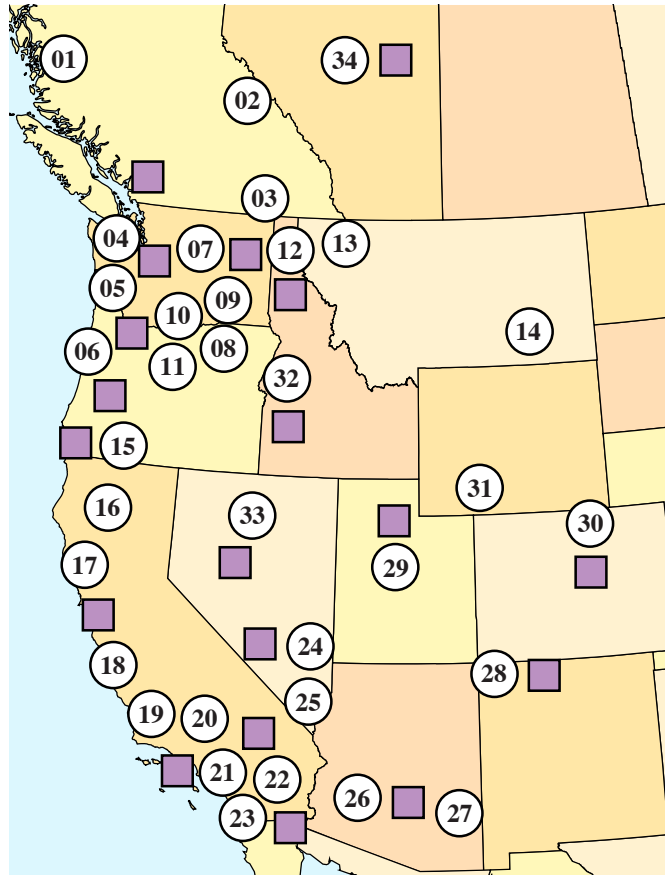


Figure 3: Notable locations in the miniWECC system. The numbered circles represent equivalent generators, and the colored squares represent the control actuators, which are utility-scale inverter-based resources.

3.1 Time-Domain Analysis

This subsection examines the effect of sweeping the tuning parameters α_1 and α_2 on the time-domain system response. The aim is to build intuition about how the control strategy responds to disturbances, and how the resulting injections affect the state trajectories. Each of the 19 participating ESSs, rated at 100 MW/200 MWh, were configured identically for simplicity. These systems may correspond either to large individual ESSs or aggregated storage clusters. We consider a total ESS power capacity of 1.9 GW, which represents about 1.8% of the overall miniWECC load. In all examples $G_{w1}(s)$ is a first-order highpass filter with a corner frequency at 0.1 Hz, and $G_{w2}(s)$ second-order with a corner near 0.01 Hz. In the α_2 path, we included 15° of phase lead centered about the *frequency regulation mode* at 0.02 Hz. As described in [44, 45], the frequency regulation mode of a power system is a very low frequency mode, typically below 0.1 Hz, in which the rotor speeds of all synchronous generation units participate. No phase compensation was introduced in the α_1 path. Lastly, the gain of each controller was held fixed at $K = 5$.

Fig. 4 shows time-domain simulations of a large nuclear plant in Arizona, G26, being tripped offline for various values of α_1 , where $\alpha_2 = 0$. This disturbance was selected because it represents a severe step change in the generation/demand balance. The lost generation corresponds to approximately 4% of the total load. The top subplot shows the difference between the rotor angle of generator G34 in Alberta and G23 in San Diego. This pair represents the maximal inter-machine angle difference observed for this disturbance. The control effort has a stabilizing effect on this angle separation. In particular, the frequency of the oscillatory component of the response rises, which indicates an increase in synchronizing torque.

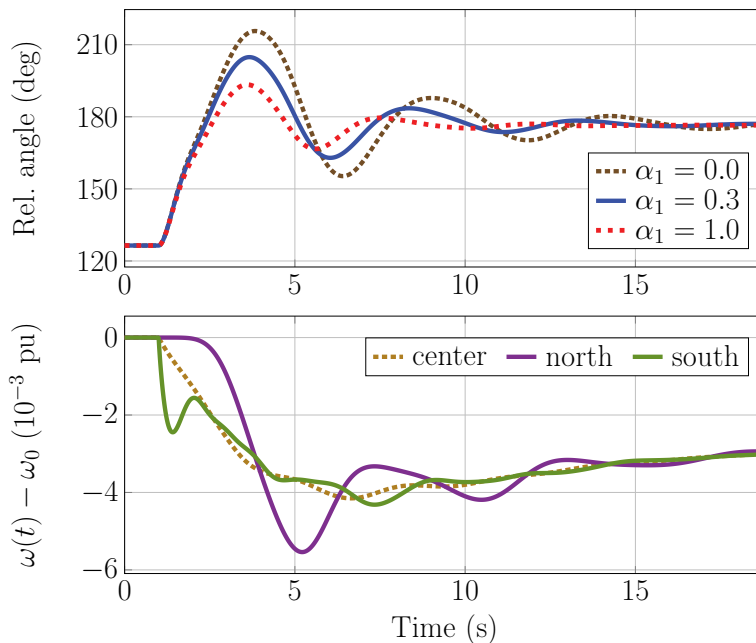


Figure 4: Time-domain simulations of generator G26 in Arizona being tripped offline for various values of α_1 , where $\alpha_2 = 0$. The top subplot shows the relative angle between generator G34 in Alberta (north) and G23 in San Diego (south). The bottom shows the speed of G23, G34, and the center of inertia in the open-loop case.

The bottom subplot of Fig. 4 shows the speed of generator G34 (Alberta) and G23 (San Diego) compared with the speed of the center of inertia for the open-loop case. Immediately following the disturbance, the speed of the generator in Alberta is slightly faster than the speed of the center of inertia, and the speed of the generator in San Diego slightly slower. This occurs because the machine in San Diego is electrically closer to the tripped generator than the average machine in the system, and the machine in Alberta farther away. Over the first swing of the transient, these relationships manifest themselves as a positive α_1 error component in Alberta and a negative α_1 component in San Diego. The top subplot of Fig. 5 shows the α_1 component of the control response, which results from passing $\alpha_1[\theta_j(t) - \bar{\theta}_j(t)]$ through the controller compensation. To mitigate the system separation in the first swing, the ESS in Alberta charges and the one in San Diego discharges. This charging modulation is shown in the bottom subplot of Fig. 5.

Fig. 6 shows time-domain simulations of the same generator trip but for the case where α_2 is swept over a range of values and $\alpha_1 = 0$. The top subplot shows the system frequency, calculated as the frequency of the center of inertia. The control effort has a stabilizing effect on the frequency response. As α_2 increases the depth of the nadir is reduced, and the frequency rebounds more quickly. The bottom subplot shows the relative angle between generator G34 in Alberta and G23 in San Diego (as in Fig. 4). By design, varying the value of α_2 does not have an impact on this angle difference. The purpose of α_2 is solely to adjust the behavior of the frequency regulation mode, which is common to all synchronous generators in the system. In situations where providing synchronizing torque at the frequency regulation mode is not required (or desirable), α_2 may be set to zero with no adverse effect on the control response over the remainder of the frequency band.

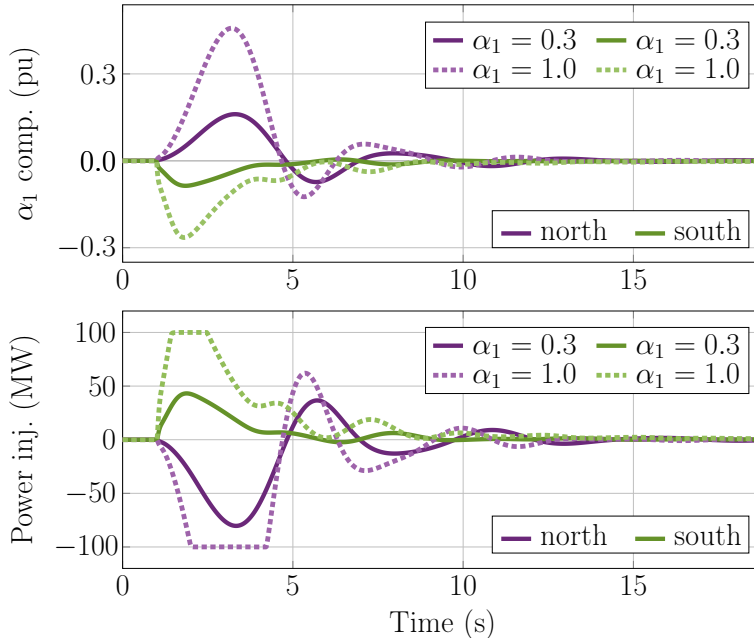


Figure 5: The control response corresponding to the time-domain simulations shown in Fig. 4. The top subplot shows the α_1 component of the control error and the bottom the injected power. The purple and green traces show the behavior of the actuators located near the load centers in Alberta (north) and San Diego (south), respectively.

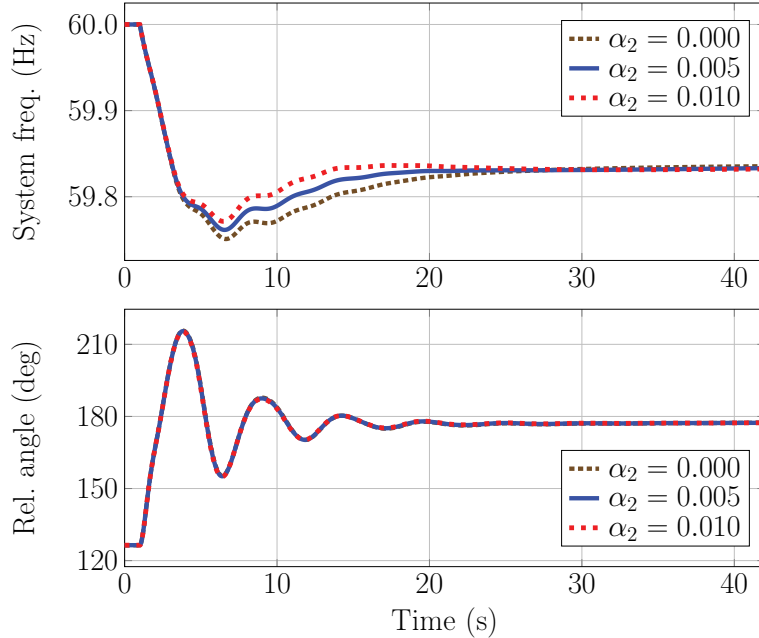


Figure 6: Time-domain simulations of generator G26 in Arizona being tripped offline for various values of α_2 , where $\alpha_1 = 0$. The top subplot shows the frequency of the center of inertia. The bottom shows the relative angle between generator G34 in Alberta (north) and G23 in San Diego (south). This angle difference does not vary with α_2 .

Fig. 7 shows the behavior of a representative controller, which is the same for each ESS in this case (when $\tilde{\theta}(t)$ is the same). The top subplot shows the α_2 component of the control response, which results from passing $\alpha_2[\tilde{\theta}(t) - \tilde{\theta}(t_0)]$ through the controller compensation. Neglecting the effects of nonideal communication, the center-of-inertia angle estimate $\tilde{\theta}(t)$ is the same for all ESSs resulting in identical α_2 components. (We consider the effects of nonideal communication in Section 4.) Following the generator trip, the speed of the center of inertia deflects downward causing $\tilde{\theta}(t)$ to decline from its initial value $\tilde{\theta}(t_0)$. This results in a negative α_2 component that causes every ESS in the system to inject power that is in phase with the error. This is shown in the bottom subplot of Fig. 7. In a practical application, the total control response would effectively be a superposition of the injections depicted in Figs. 5 and 7.

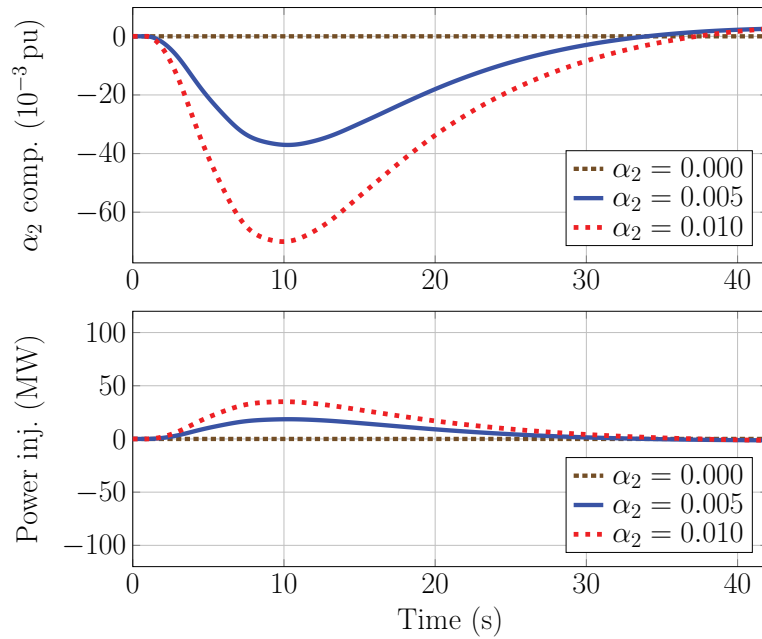


Figure 7: The control response corresponding to the time-domain simulations shown in Fig. 6. The top subplot shows the α_2 component of the control error and the bottom the injected power. In this case all of the controllers synthesize identical estimates of $\tilde{\theta}(t)$, so $\alpha_2[\tilde{\theta}(t) - \tilde{\theta}(t_0)]$ is the same for each actuator.

3.2 Tuning Considerations

Linear analysis allows us to develop criteria that are *necessary but not sufficient* for ensuring acceptable transient stability control performance. For example, theory dictates that positive synchronizing torque drives the electromechanical modes of oscillation upward in the complex plane, indicating an increase in frequency. Furthermore, the open-loop frequency response for each actuator must obey the Nyquist stability criterion. Fig. 8(a) shows how the eigenvalues of the miniWECC respond when α_1 is swept over the interval $[0, 1]$ uniformly for all actuators, where $\alpha_2 = 0$ and $K = 30$. The electromechanical modes that are responsive to the control are either pushed directly upward, indicating pure synchronizing torque, or up and to the left, indicating a combination of damping and synchronizing. The frequency regulation mode, marked with a red triangle, is not sensitive to α_1 . Conversely, Fig. 8(b) shows that as α_2 is swept over $[0, 0.1]$, the frequency regulation mode moves upward while the inter-area and local modes are unaffected. The phase lead introduced in the α_2 path ensures that the angle of departure of the frequency regulation mode is directly vertical, as opposed to slightly to the right. Recall from root locus analysis that the angle of departure is the initial angle at which a closed-loop pole travels in response to a change in the swept parameter [46].

Fig. 9 shows the open-loop frequency response between a change in P_{ref} and the controller output p_s for the ESS located in British Columbia. The traces correspond to various values of α_1 , where $\alpha_2 = 0.01$ is held fixed. If the controller were to provide pure synchronizing torque across its entire bandwidth, then the phase response would transition through -90° at each resonant frequency. We observe that the North-South A mode just above 0.20 Hz is not strongly observable in the amplitude response. At this frequency, the phase is near 0° indicating that the controller provides more damping torque than synchronizing. At the other two highlighted resonances, the North-South B mode near 0.35 Hz and the British Columbia mode near 0.63 Hz, the phase

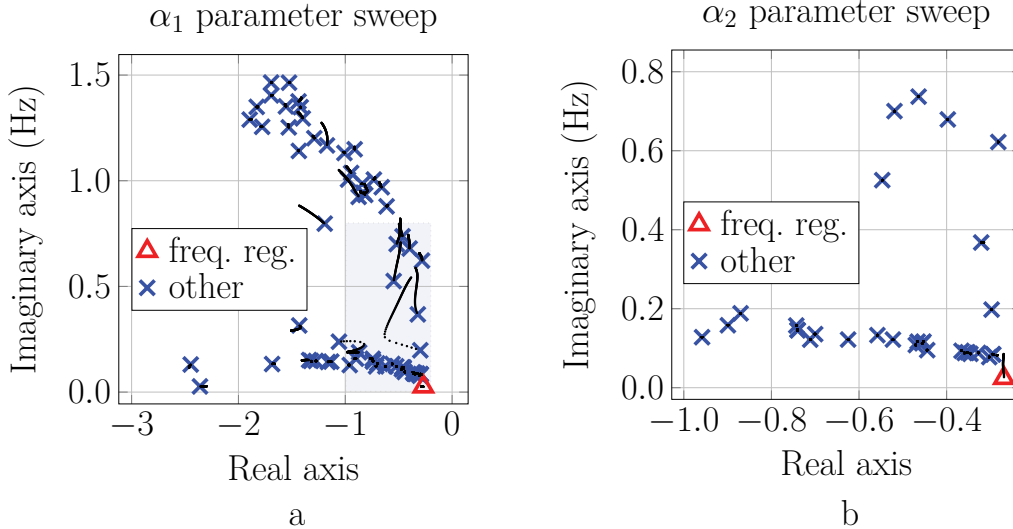


Figure 8: Sensitivity of the system oscillatory modes to the tuning parameters. The frequency regulation mode, represented by the red triangle, is much more sensitive to changes in α_2 than α_1 . The converse is true for the other modes. The shaded patch in (a) shows the axis range of (b).

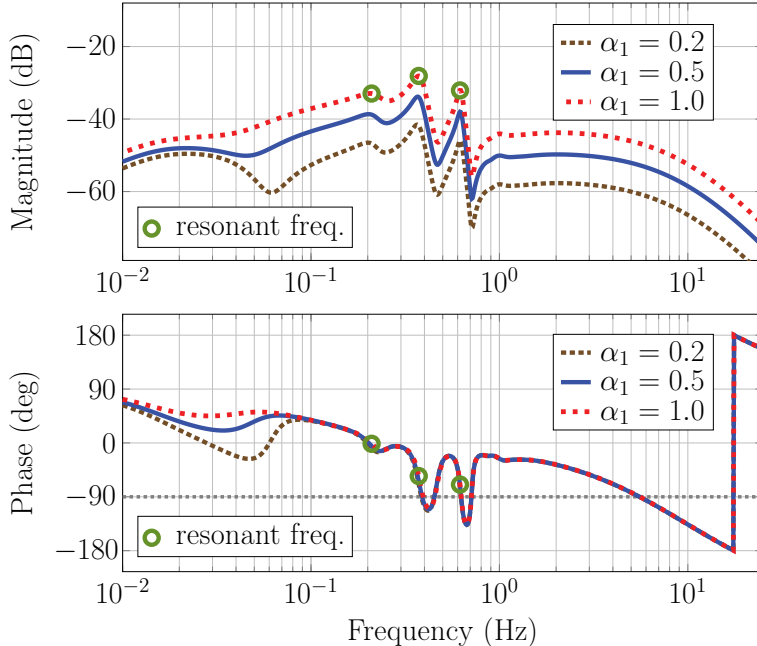


Figure 9: The open-loop frequency response between a change in P_{ref} and p_s for the ESS located in British Columbia, where $\alpha_2 = 0.01$ for all traces. At a given frequency, the phase response indicates whether the controller provides damping torque (0°), synchronizing torque (-90°), or some combination thereof.

response is much closer to -90° , indicating a stronger synchronizing response. Although Fig. 9 corresponds to an individual actuator, these observations mirror the angles of departure shown in Fig. 8. Varying α_1 serves to adjust the amplitude response over the range of frequencies above the frequency regulation mode. In contrast, varying α_2 adjusts the amplitude response in the neighborhood of the frequency regulation mode. Fig. 10 shows the open-loop frequency response of the same ESS for various values of α_2 , where $\alpha_1 = 1.0$ for all traces. Because the α_2 deviations $\tilde{\theta}(t) - \tilde{\theta}(t_0)$ may be considerably larger than the α_1 deviations $\theta_j(t) - \tilde{\theta}_j(t)$, the tuning parameters should be set such that $\alpha_2 \ll \alpha_1$. In the analysis presented in Section 4, we set these parameters to $\alpha_1 = 1.0$ and $\alpha_2 = 0.01$ for all actuators.

While α_1 and α_2 are useful tools for shaping the amplitude response, they have a limited impact on the phase. To address this limitation, a lead-lag compensation stage is included in each branch of the control structure shown in Fig. 1. As a consequence of the Nyquist stability criterion, a guiding principle when tuning the controller is to keep the phase response within $\pm 90^\circ$ from dc through the position of the highest resonant frequency. This ensures that critical frequencies, where the phase response reaches -180° , will not coincide with any resonant peaks in the amplitude response [40]. A second principle is to aim for a phase response that transitions through -90° at the resonant frequencies [47]. This ensures that the controller primarily provides synchronizing torque, which it must if it is to improve transient stability. As discussed above, if the phase response does not transition through -90° at a resonant peak, then it is desirable for it fall between $[-90^\circ, 0^\circ]$ so that it provides a combination of synchronizing and damping torque [48].

The broad hump in the amplitude response near 0.02 Hz shown in Figs. 9 and 10 corresponds

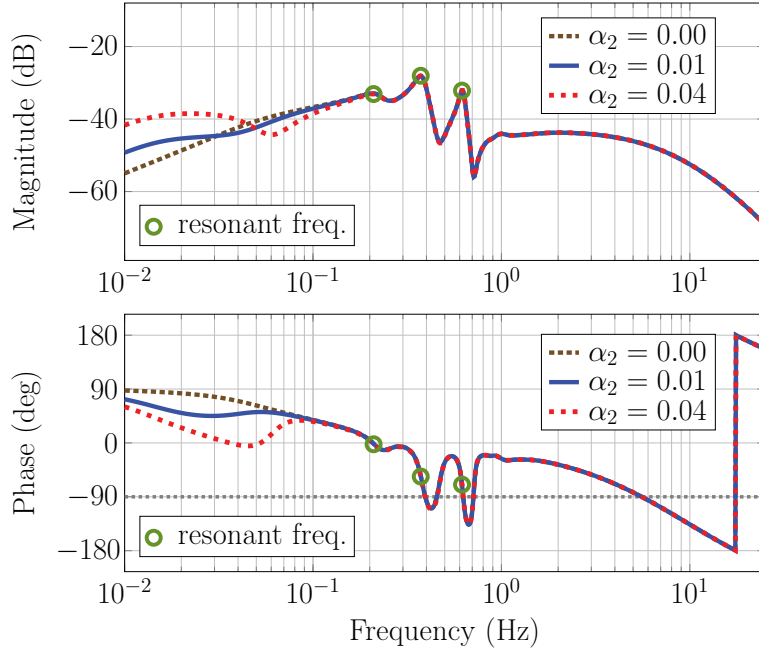


Figure 10: The open-loop frequency response between a change in P_{ref} and p_s for the ESS located in British Columbia, where $\alpha_1 = 1.0$ for all traces. At a given frequency, the phase response indicates whether the controller provides damping torque (0°), synchronizing torque (-90°), or some combination thereof.

to the frequency regulation mode. Although it manifests itself as a mild resonance, the tuning considerations are somewhat different than for the inter-area modes. Time- and frequency-domain objectives must be given equal weight. Values of α_2 larger than those shown in Fig. 10 may cause the controller to interfere with turbine governing and/or automatic generation control (AGC) during transient disturbances. They may also deprive the α_1 component of the control error of the modulation headroom necessary to keep individual generators in synchronism with the center of inertia. Thus, as stated above, it is advisable to ensure that $\alpha_2 \ll \alpha_1$. Rather than tuning the control response in relation to the frequency regulation mode exclusively using Bode diagrams, it may be preferable to incorporate a combination of modal sensitivity analysis, as shown in Fig. 8, and time-domain simulation. The compensation should be configured such that the angle of departure of the frequency regulation mode is as close to vertical as possible as α_2 increases. This ensures that the controller provides synchronizing torque at the modal frequency [48].

The tuning considerations discussed here are applicable primarily to large interconnections. In systems where an individual machine makes up a substantial percentage of the overall system inertia/capacity, different tunings may be necessary. In particular, the relative value of α_1 to α_2 may be somewhat different, with larger values of α_2 potentially being viable in some cases.

4 N-1 Contingency Analysis

In this section, we conduct N-1 contingency analysis to study the impact of the control strategy for a range of disturbances. This analysis serves as an example of the type of simulation protocol that would be required to verify that a set of actuators, tuned in a particular way, yields acceptable control performance at a given operating point. We simulated 28 generator trips, 80 transmission line faults (three-phase bolted, cleared after 6 cycles), and 19 losses of load (50 % of apparent power). Each contingency was simulated three times: in open loop, closed loop, and in closed loop with nonideal communication. We employed a statistical communication model that accounts for delays, jitter, and measurement noise. The expected delay for each sensor was uniformly distributed between 67 and 250 ms. The high end of this range is more than double the maximum value reported in a recent real-world experiment (69–113 ms) [40].

The actuators were placed and configured as in Section 3.1 with a 100 MW ESS located at each of the 19 load centers. The tuning parameters and gain were set uniformly for all actuators such that $\alpha_1 = 1.0$, $\alpha_2 = 0.01$, and $K = 10$. These example values were selected based on the time-domain sensitivity analysis performed in Section 3.1 and the frequency-domain tuning considerations in Section 3.2. As a result of the device power rating, each actuator can inject (or withdraw) a maximum of 100 MW. During a severe disturbance, actuators in different parts of the system respond differently, with some injecting and some withdrawing power over the first swing of the transient.

Table 2 provides a summary of the results. It compares the open-loop case to the closed-loop case with nonideal communication. Here the *first swing* of the generator response is defined as the magnitude of the initial extremum of $\Delta\delta_i$ following the disturbance. The control strategy reduced the magnitude of 99.4 % of first swings by an average of 17.3 %. For the very small fraction of first swings (0.6 %) that did not decline, the average increase was 1.1 %. The largest observed improvement in the magnitude of the first swing was -21.37° , while the worst-case degradation was 0.95° .

The worst-case response was observed at generator G31 in Wyoming in response to a fault on the California-Oregon Intertie. In the case with nonideal communication, this angle response represented the worst first-swing degradation both in absolute terms, as measured in degrees, and on a percentage basis. Fig. 11 shows the angle and speed trajectories for G31 with respect to the center of inertia in response to the fault. In the closed-loop case with ideal communication, the generator response is effectively the same as in the open-loop case; however, in the case with nonideal communication, it is degraded slightly. The scale of the plots is zoomed in to show the differences between the observed trajectories. The magnitude of the first-swing angle response

Table 2: N-1 Contingency Analysis First Swing Summary

Event	Number of first swings	Improvement rate (%)	Mean decrease in $\Delta\delta$ (%)
Loss of load	646	99.7	18.0
Gen. trip	924	99.5	18.4
Fault/line clearing	2720	99.3	16.8
Total	4290	99.4	17.3

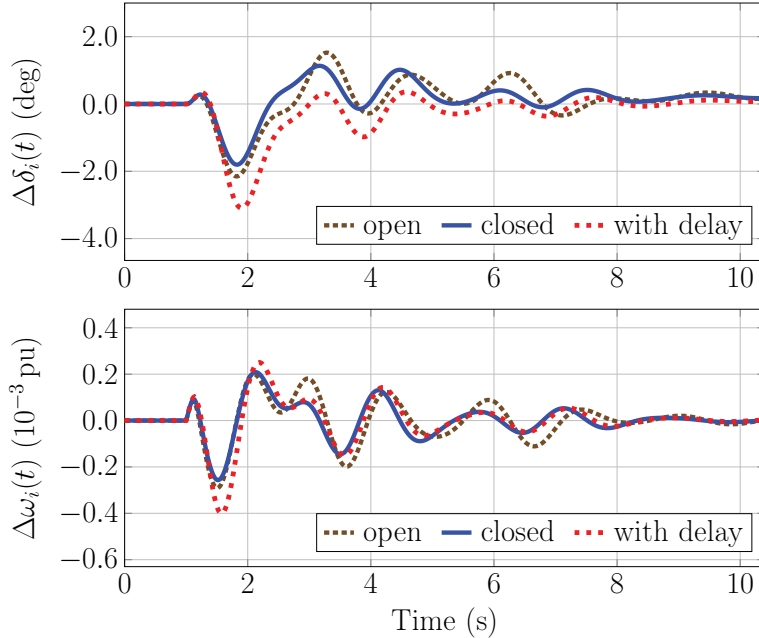


Figure 11: Simulated state trajectories for generator G31 in Wyoming in response to a 6-cycle fault on the California-Oregon Intertie. This represents the worst-case degradation in the first swing observed in the N-1 contingency analysis.

increased by 0.95° , and the speed response by 1×10^{-4} pu. This generator is far away from the fault and not at serious risk of instability for this disturbance.

In these examples, the IBRs are located at the major load centers, as shown in Fig. 3. Since much of the power generated in Montana and Wyoming is exported elsewhere, there are no IBRs modeled in either of those states. The response of generator G31 could be improved by placing a control actuator near it. This analysis indicates that even in the case where a generator is far away (electrically) from the IBRs, it frequently experiences a moderate improvement in its first-swing transient response as a result of the control. In cases where the response does not improve, it does not appear to be significantly degraded.

4.1 In-Depth Fault Analysis

To provide analysis of a representative contingency, we study a 9-cycle fault near generator G34 in Alberta. For this fault, the control strategy improves the critical clearing time from 6 cycles to 10 cycles. Fig. 12 plots the state response in the time-domain, where the upper subplot shows the voltage magnitude at the faulted bus. The lower subplots show the LTI speed deviations (i.e., $\omega(t) - \omega_0$) for G34 in Alberta, G23 in San Diego, and the center of inertia. For the closed-loop cases, the results with delay effectively overlap those without. In open loop, the generator in Alberta loses synchronism. When this occurs, G23 in San Diego begins oscillating against the center of inertia. In practice, out-of-step or overspeed protection would likely trip the critical unit in Alberta before it lost synchronism. This protection may mitigate the oscillations observed in San Diego. The bottom subplot shows the speed deviations in closed loop, including the effect of delays and noise. In this case, the generator in Alberta remains synchronized and the oscillations in San Diego subside.

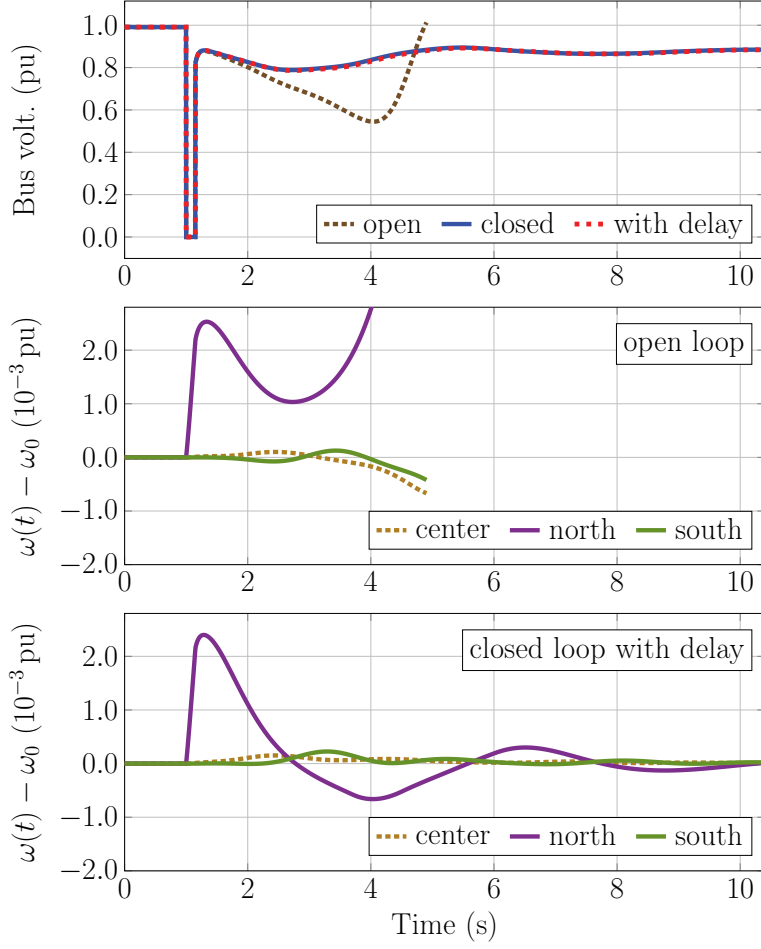


Figure 12: Time-domain simulations of a 9-cycle fault near generator G34 in Alberta. The top subplot shows the voltage magnitude at the faulted bus. The bottom two subplots show the LTI speed deviations of G34 in Alberta (north) and G23 in San Diego (south) compared with the center of inertia.

We can gain additional insight into this fault by studying the system response in the angle domain. The phase portraits shown in Fig. 13 plot the LTV speed deviations $\Delta\omega_i$ versus $\Delta\delta_i$ for the two machines discussed above. In open loop, the curves do not arrive at a post-disturbance equilibrium; however, in closed loop they do. This indicates that the control action expands the region of attraction to encompass the point in the plane where each generator resides immediately after the fault.

Using this perspective, we can also compare the accelerating areas. Under the classical model, the accelerating power of the i th machine in the center-of-inertia reference frame is

$$\Delta P_a^i(t) = P_m^i(t) - P_e^i(t) - \frac{H_i}{H_T} \left[\sum_{k \in \mathcal{K}} P_m^k(t) - P_e^k(t) \right], \quad (31)$$

where \mathcal{K} is the set of all online synchronous machines [13]. The top subplot of Fig. 14 shows the accelerating power of G34 in Alberta as a function of $\Delta\delta_i$, and the bottom the integral of ΔP_a^i over $\Delta\delta_i$. Assuming the damping constants are negligible, this integral yields the kinetic energy

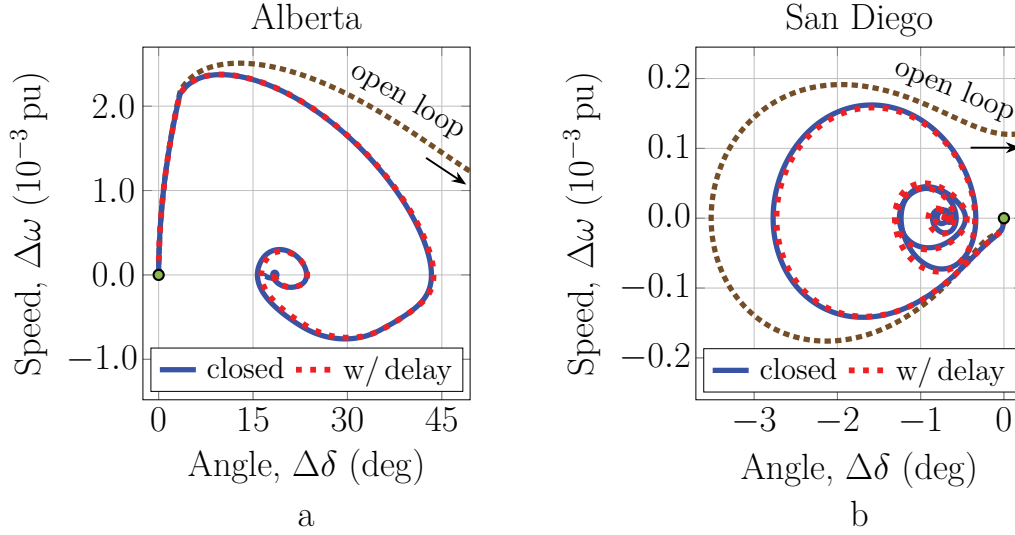


Figure 13: Phase plane analysis in the center-of-inertia reference frame for a 9-cycle fault near generator G34 in Alberta. Subfigure (a) shows the behavior of G34 in Alberta, and (b) G23 in San Diego. All curves begin at the origin.

in the center-of-inertia reference frame $H_i \Delta\omega_i^2$. In open loop, the decelerating area is insufficient to cancel the accelerating area, and the machine pulls away from the stable equilibrium. In the bottom subplot, this manifests itself as the failure of the kinetic energy curve to reach the x -axis, i.e., zero energy. The control action reduces the accelerating area and expands the decelerating area, as shown in blue. This allows the kinetic energy curve to reach the x -axis, where the machine begins its second swing.

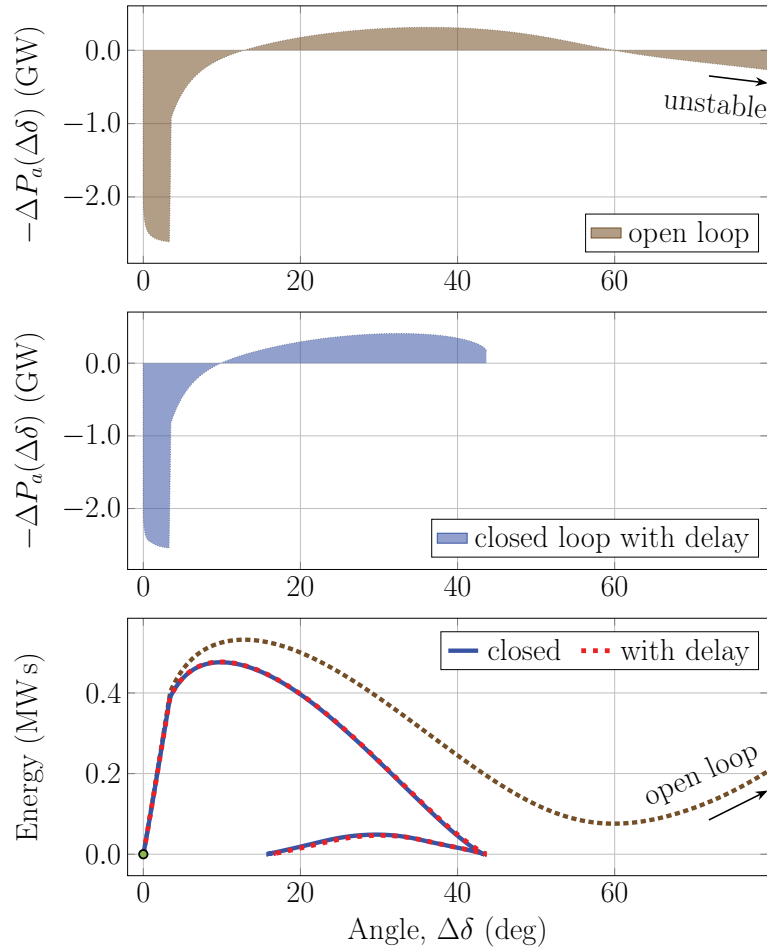


Figure 14: Accelerating power analysis in the center-of-inertia reference frame for a 9-cycle fault near generator G34 in Alberta. The top subplot shows the accelerating and decelerating areas in open and closed loop. The bottom subplot shows the integral of accelerating power as a function of $\Delta\delta$.

5 Simplified Path Rating Study

In practice, the type of contingency analysis presented in Section 4 plays an important role in establishing ratings for stability-limited transmission corridors. One such corridor in the Western Interconnection is the California-Oregon Intertie. By choosing a plausible critical contingency for this corridor, we can estimate the impact of the control strategy on the transfer limit. With north-to-south flows, we will assume the critical contingency is a trip of G18 in the miniWECC, a large gas-fired generator near the southern end of the intertie. At the initial operating point G18 supplies 5 GW of real power, or roughly 4.5 % of the system load. Thus, the interface flows must change substantially in order for the system to remain stable following the disturbance. In cases where the system stabilized, the flow on the California-Oregon Intertie was observed to increase by more than 1 GW following the disturbance. This is expected because the loss of G18 results in a generation deficit in California. When the power transfer on the intertie exceeds its maximum safe level, the system lacks the stiffness to accommodate the sudden increase in flows caused by the generation trip. The voltage magnitudes at the ends of the intertie fall precipitously, and the power transfer never stabilizes. When this occurs, the system begins to separate with the Pacific Northwest and the northern half of the system pulling away from California and the southern half.

For this contingency, we find that the maximum transfer that yields a stable response in the open-loop case is 5.3 GW. To determine this limit, we incrementally increased the loading in California and redispatched the generation in the Pacific Northwest. In the closed-loop case, the controllers produce supplemental synchronizing torque by reducing deviations in the power angle across the intertie. Immediately following the generation trip, the energy storage systems in California discharge, helping to offset the loss of G18. The storage systems in the Pacific Northwest and Canada charge, which increases the load in the northern half of the system in an effort to reduce north-to-south intertie flows. In closed loop, the transfer limit increases from 5.3 GW to 6.1 GW. Hence, in this example, 1.9 GW of energy storage is able to increase the transfer limit by roughly 800 MW. In reality, this result would need to be confirmed for various operating conditions and multiple critical contingencies. The intent of this analysis is not to identify the path rating for a particular operating condition, but rather to gauge the magnitude and sign of the change in the path rating as a result of control. Fig. 15 shows time-domain simulation results for a trip of G18 when the steady-state active power transfer on the intertie is 6.1 GW. As explained above, in the open-loop case the power transfer never stabilizes after the disturbance. When the system goes unstable the power flow fails to converge, halting the simulation. In the closed-loop case, the control action allows the system to safely reach a post-disturbance equilibrium.

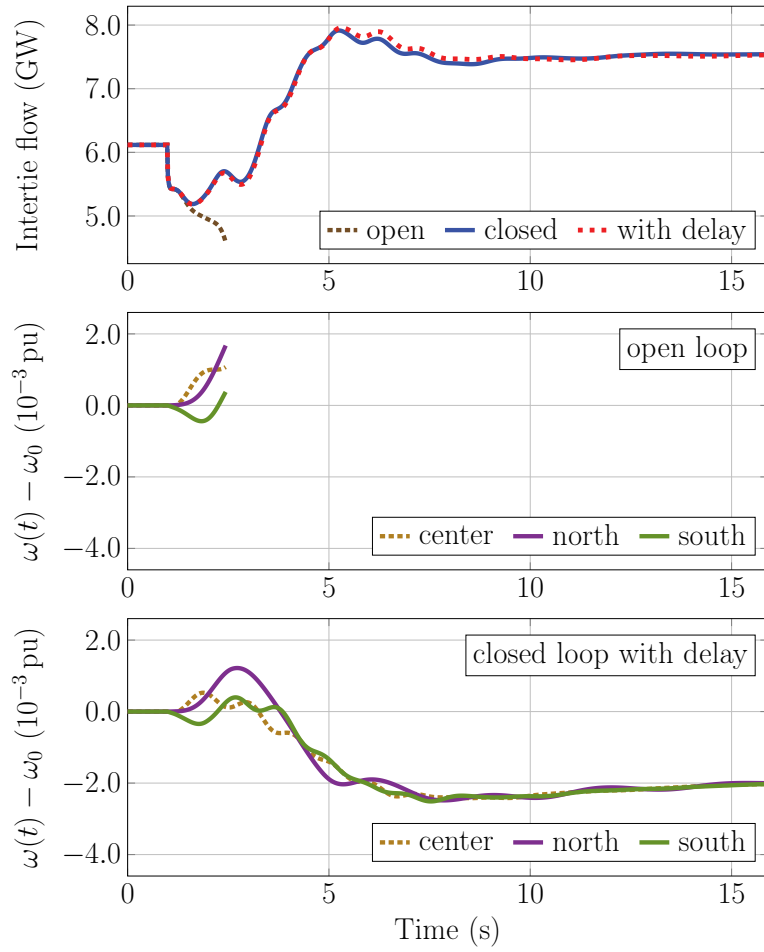


Figure 15: Time-domain simulations for a trip of generator G18 near the southern end of the California-Oregon Intertie. The upper subplot shows the active power flow on the intertie from north to south. The bottom two subplots show the LTI speed deviations of G34 in Alberta (north) and G23 in San Diego (south) compared with the center of inertia.

6 Conclusion

In this paper, we developed and demonstrated a control strategy that modulates the active power injected by inverter-based resources. For testing, we employed a reduced-order dynamic model of the Western Interconnection. The key points can be summarized as follows:

- The proposed method was based on a time-varying representation of the equations of motion for a synchronous machine.
- The control strategy uses IBRs to inject active power into the system that is in phase with the LTV angle deviations.
- For each IBR, the injection drives the bus voltage angle toward a desired trajectory that tracks the angle of the center of inertia.
- The feedback signals are constructed using bus voltage phasor data collected from wide-area measurement systems.
- While generator data may be used if it is available, it is not required to produce an estimate of the center-of-inertia states that is sufficiently accurate for control.
- This control strategy improves system reliability by helping to keep each generator in synchronism with the center of inertia.
- In addition, this approach can increase capacity utilization on stability-limited transmission corridors, allowing existing infrastructure to be used more efficiently.

We are currently conducting ongoing research examining the performance of the developed control strategy in relation to alternative technologies/approaches. This work is also exploring techniques and considerations for setpoint management, i.e., when and how to update the constants in (24) as the dispatch pattern changes. Future work will investigate improved methods for characterizing transient stability margins in nonlinear systems.

References

- [1] P. M. Anderson and B. K. LeReverend, "Industry experience with special protection schemes," *IEEE Trans. Power Syst.*, vol. 11, pp. 1166–1179, Aug. 1996.
- [2] J. Zaborszky, K. Prasad, and Keh-Wen Whang, "Stabilizing control in emergencies—Part 2: Control by local feedback," *IEEE Trans. Power App. Syst.*, vol. PAS-100, pp. 2381–2389, May 1981.
- [3] D. Trudnowski, D. Kosterev, and J. Wold, "Open-loop PDCI probing tests for the western North American power system," in *Proc. IEEE Power Energy Soc. Gen. Meeting*, pp. 1–5, July 2014.
- [4] Y. Xue, T. Van Cutsem, and M. Ribbens-Pavella, "Extended equal area criterion justifications, generalizations, applications," *IEEE Trans. Power Syst.*, vol. 4, pp. 44–52, Feb. 1989.
- [5] P. Varaiya, F. F. Wu, and Rong-Liang Chen, "Direct methods for transient stability analysis of power systems: Recent results," *Proc. IEEE.*, vol. 73, pp. 1703–1715, Dec. 1985.
- [6] Hsiao-Dong Chiang, Chia-Chi Chu, and G. Cauley, "Direct stability analysis of electric power systems using energy functions: Theory, applications, and perspective," *Proc. IEEE.*, vol. 83, pp. 1497–1529, Nov. 1995.
- [7] P. C. Magnusson, "The transient-energy method of calculating stability," *Trans. AIEE*, vol. 66, pp. 747–755, Jan. 1947.
- [8] T. Athay, R. Podmore, and S. Virmani, "A practical method for the direct analysis of transient stability," *IEEE Trans. Power App. Syst.*, vol. PAS-98, pp. 573–584, Mar. 1979.
- [9] A. R. Bergen and D. J. Hill, "A structure preserving model for power system stability analysis," *IEEE Trans. Power App. Syst.*, vol. PAS-100, pp. 25–35, Jan. 1981.
- [10] V. Vittal, *Power system transient stability using the critical energy of individual machines*. Retrospective theses and dissertations, Iowa State University, 1982.
- [11] I. A. Hiskens and D. J. Hill, "Energy functions, transient stability and voltage behaviour in power systems with nonlinear loads," *IEEE Trans. Power Syst.*, vol. 4, pp. 1525–1533, Nov. 1989.
- [12] M. A. Pai, *Energy Function Analysis for Power System Stability*. Power Electronics and Power Systems, Springer US, 1989.
- [13] A. Michel, A. Fouad, and V. Vittal, "Power system transient stability using individual machine energy functions," *IEEE Trans. Circuits Syst.*, vol. 30, pp. 266–276, May 1983.
- [14] P. Kundur, N. Balu, and M. Lauby, *Power system stability and control*. EPRI Power Systems Engineering, McGraw-Hill, 1994.
- [15] G. A. Maria, C. Tang, and J. Kim, "Hybrid transient stability analysis," *IEEE Trans. Power Syst.*, vol. 5, pp. 384–393, May 1990.

- [16] Y. Mansour, E. Vaahedi, A. Y. Chang, B. R. Corns, B. W. Garrett, K. Demaree, T. Athay, and K. Cheung, "BC Hydro's on-line transient stability assessment (TSA) model development, analysis and post-processing," *IEEE Trans. Power Syst.*, vol. 10, pp. 241–253, Feb. 1995.
- [17] S. E. Stanton, C. Slivinsky, K. Martin, and J. Nordstrom, "Application of phasor measurements and partial energy analysis in stabilizing large disturbances," *IEEE Trans. Power Syst.*, vol. 10, pp. 297–306, Feb. 1995.
- [18] T. L. Vu and K. Turitsyn, "Lyapunov functions family approach to transient stability assessment," *IEEE Trans. Power Syst.*, vol. 31, no. 2, pp. 1269–1277, 2016.
- [19] P. Ju, H. Li, C. Gan, Y. Liu, Y. Yu, and Y. Liu, "Analytical assessment for transient stability under stochastic continuous disturbances," *IEEE Trans. Power Syst.*, vol. 33, no. 2, pp. 2004–2014, 2018.
- [20] A. Iravani and F. de León, "Real-time transient stability assessment using dynamic equivalents and nonlinear observers," *IEEE Trans. Power Syst.*, vol. 35, no. 4, pp. 2981–2992, 2020.
- [21] O. Romay, R. Martinez-Parrales, and C. R. Fuerte-Esquivel, "Transient stability assessment considering hard limits on dynamic states," *IEEE Trans. Power Syst.*, pp. 1–1, 2020.
- [22] H. Wang, Q. Wang, and Q. Chen, "Transient stability assessment model with improved cost-sensitive method based on the fault severity," *IET Gener. Transm. Distrib.*, vol. 14, no. 20, pp. 4605–4611, 2020.
- [23] G. C. Zweigle and V. Venkatasubramanian, "Wide-area optimal control of electric power systems with application to transient stability for higher order contingencies," *IEEE Trans. Power Syst.*, vol. 28, pp. 2313–2320, Aug. 2013.
- [24] P. Bhui and N. Senroy, "Real-time prediction and control of transient stability using transient energy function," *IEEE Trans. Power Syst.*, vol. 32, pp. 923–934, Mar. 2017.
- [25] M. Abdi-Khorsand and V. Vittal, "Identification of critical protection functions for transient stability studies," *IEEE Trans. Power Syst.*, vol. 33, pp. 2940–2948, May 2018.
- [26] Z. Yao, "A control-oriented energy function for generation shedding determination for transient stability control," *IEEE Trans. Power Syst.*, vol. 34, pp. 413–421, Jan. 2019.
- [27] Y. Guo, D. J. Hill, and Y. Wang, "Global transient stability and voltage regulation for power systems," *IEEE Trans. Power Syst.*, vol. 16, pp. 678–688, Nov. 2001.
- [28] T. Li, G. Ledwich, Y. Mishra, J. H. Chow, and A. Vahidnia, "Wave aspect of power system transient stability—Part II: Control implications," *IEEE Trans. Power Syst.*, vol. 32, pp. 2501–2508, July 2017.
- [29] M. Ghandhari, G. Andersson, and I. A. Hiskens, "Control lyapunov functions for controllable series devices," *IEEE Trans. Power Syst.*, vol. 16, pp. 689–694, Nov. 2001.
- [30] M. H. Haque, "Evaluation of first swing stability of a large power system with various FACTS devices," *IEEE Trans. Power Syst.*, vol. 23, pp. 1144–1151, Aug. 2008.

- [31] K. Kawabe and A. Yokoyama, “Improvement of angle and voltage stability by control of batteries using wide-area measurement system in power systems,” in *IEEE PES Innovative Smart Grid Tech. Europe*, pp. 1–7, Oct. 2012.
- [32] R. Yousefian, R. Bhattarai, and S. Kamalasadani, “Transient stability enhancement of power grid with integrated wide area control of wind farms and synchronous generators,” *IEEE Trans. Power Syst.*, vol. 32, pp. 4818–4831, Nov. 2017.
- [33] R. T. Elliott, P. Arabshahi, and D. S. Kirschen, “A generalized PSS architecture for balancing transient and small-signal response,” *IEEE Trans. Power Syst.*, pp. 1–1, 2019.
- [34] R. Elliott, *Trajectory tracking wide-area control for power systems*. Doctoral dissertation, Electrical and Computer Engineering, University of Washington, 2020.
- [35] K. Tsakalis and P. Ioannou, *Linear time-varying systems: Control and adaptation*. Electrical engineering: Controls, Prentice Hall, 1993.
- [36] C. J. Távora and O. J. M. Smith, “Characterization of equilibrium and stability in power systems,” *IEEE Trans. Power App. Syst.*, vol. PAS-91, pp. 1127–1130, May 1972.
- [37] A. G. Phadke, J. S. Thorp, and M. G. Adamiak, “A new measurement technique for tracking voltage phasors, local system frequency, and rate of change of frequency,” *IEEE Trans. Power App. Syst.*, vol. PAS-102, no. 5, pp. 1025–1038, 1983.
- [38] NASPI Engineering Analysis Task Team, “Phase angle calculations: Considerations and use cases.” Technical paper, 2016. Accessed: Oct 1, 2020.
- [39] R. T. Elliott, A. Ellis, P. Pourbeik, J. J. Sanchez-Gasca, J. Senthil, and J. Weber, “Generic photovoltaic system models for WECC–A status report,” in *Proc. IEEE Power Energy Soc. Gen. Meeting*, pp. 1–5, July 2015.
- [40] B. J. Pierre, F. Wilches-Bernal, D. A. Schoenwald, R. T. Elliott, D. J. Trudnowski, R. H. Byrne, and J. C. Neely, “Design of the Pacific DC Intertie wide area damping controller,” *IEEE Trans. Power Syst.*, vol. 34, no. 5, pp. 3594–3604, 2019.
- [41] D. Dolezilek and L. Hussey, “Requirements or recommendations? Sorting out NERC CIP, NIST, and DOE cybersecurity,” in *Proc. Annual Conf. Protective Relay Eng.*, pp. 328–333, 2011.
- [42] B. Pierre, R. Elliott, D. Schoenwald, J. Neely, R. Byrne, D. Trudnowski, and J. Colwell, “Supervisory system for a wide area damping controller using PDCI modulation and real-time PMU feedback,” in *Proc. IEEE Power Energy Soc. Gen. Meeting*, pp. 1–5, 2016.
- [43] J. H. Chow and K. W. Cheung, “A toolbox for power system dynamics and control engineering education and research,” *IEEE Trans. Power Syst.*, vol. 7, pp. 1559–1564, Nov. 1992.
- [44] R. Grondin, I. Kamwa, L. Soulieres, J. Potvin, and R. Champagne, “An approach to PSS design for transient stability improvement through supplementary damping of the common low-frequency,” *IEEE Trans. Power Syst.*, vol. 8, pp. 954–963, Aug. 1993.

- [45] F. Wilches-Bernal, J. H. Chow, and J. J. Sanchez-Gasca, "A fundamental study of applying wind turbines for power system frequency control," *IEEE Trans. Power Syst.*, vol. 31, pp. 1496–1505, Mar. 2016.
- [46] C. A. Stapleton, "Root-locus study of synchronous-machine regulation," *Proceedings of the Institution of Electrical Engineers*, vol. 111, no. 4, pp. 761–768, 1964.
- [47] G. J. W. Dudgeon, W. E. Leithead, A. Dyśko, J. O'Reilly, and J. R. McDonald, "The effective role of AVR and PSS in power systems: Frequency response analysis," *IEEE Trans. Power Syst.*, vol. 22, pp. 1986–1994, Nov. 2007.
- [48] P. Pourbeik and M. J. Gibbard, "Damping and synchronizing torques induced on generators by FACTS stabilizers in multimachine power systems," *IEEE Trans. Power Syst.*, vol. 11, no. 4, pp. 1920–1925, 1996.